Kinematics of the southwestern U.S. deformation zone inferred from GPS motion data

Annemarie G. Bos and Wim Spakman
Faculty of Earth Sciences, Utrecht University, Utrecht, Netherlands

Received 13 August 2003; revised 2 February 2005; accepted 11 April 2005; published 16 August 2005.

[1] We have estimated the surface deformation field of the southwestern U.S. deformation zone in terms of the velocity gradient field and surface creep simultaneously by inversion of 497 geodetic velocities. The model shows aseismic fault motion consistent with aseismic creep measurements and a sense of motion consistent with geological observations. We deduce that our surface deformation field shows distributed deformation in a zone around the faults containing shear strains and rotations. The eastern California shear zone acts as a distinct fault zone bounded by more rigid blocks. The faults within the zone partition the shear motion, while right-lateral shear strain rates and clockwise rotations are concentrated between the bounding faults. In the same way, the San Jacinto and southern San Andreas faults act as bounding faults of a fault zone. The Mojave Desert is dominated by right-lateral shear, whereas the western Transverse Ranges (WTR) is subjected to contraction. We find significant localization of deformation east of the San Andreas fault between the Transverse Ranges and the San Francisco Bay. We attribute this to a relative rigidity contrast across the fault of $\sim$1.8. Finally, a moment deficit analysis shows an accumulation of moment deficit between 1973 and 2000 corresponding to a M_w = 6.1–6.3 earthquake along the San Andreas fault just north of the Big Bend, around the Imperial and southern San Andreas faults, and in the San Francisco Bay area along the Hayward and southern Calaveras faults.

Citation: Bos, A. G., and W. Spakman (2005), Kinematics of the southwestern U.S. deformation zone inferred from GPS motion data, *J. Geophys. Res.*, *110*, B08405, doi:10.1029/2003JB002742.

1. Introduction

[2] In the southwestern United States, the boundary between the Pacific and North American plates comprises a broad zone of deformation portraying a variety of distinct deformation styles and regions of complex tectonics (e.g., Transverse Ranges, eastern California shear zone). An important constraint on the present-day tectonics in this region is an accurate description of the velocity gradient field since this field provides important kinematic boundary conditions for dynamic modeling [e.g., *England and Houseman*, 1989; *Jackson and Molnar*, 1990], as well as a means to estimate moment deficits used for seismic hazard analysis [*Working Group on California Earthquake Prediction* (WGCEP), 1995]. Space geodetic techniques, particularly the Global Positioning System (GPS), now provide a great source of information about the patterns and rates of deformation across spatial scales of order 10 to 1000 km. Throughout the southwestern U.S. deformation zone, for example, continuously operating networks of GPS stations have been in operation since the mid-1990s (e.g., International GPS Service (IGS) [*Beutler et al.*, 1994], Precision GPS Geodetic Array/Southern California Integrated GPS Network (PGGA/SCIGN) [*Bock et al.*, 1997; http://reason.scign.org], Bay Area Regional Deformation Network (BARD) [e.g., *King et al.*, 1995], The Basin and Range Geodetic Network (BARGEN) [e.g., *Bennett et al.*, 1998; *Wernicke et al.*, 2000]). Further densification is provided by the many campaign sites from which data have become readily available [e.g., *Bennett et al.*, 1997; *Dixon et al.*, 2000a, 2000b; *Gan et al.*, 2000; *Miller et al.*, 2001; *Shen et al.*, 1996; *Thatcher et al.*, 1999]. Recently, *Bennett et al.* [1999, 2002, 2003] integrated data from a large number of the continuous and campaign networks in the southwestern United States to obtain a data set within a single reference frame.

[3] Because space geodetic positioning techniques provide velocity estimates at specific points in space, and the density of available points is quite variable depending on the region and scale of investigation (kilometers to hundreds of kilometers), resolution of the spatially continuous velocity gradient tensor field depends heavily on the number and distribution of available stations. Most interpretation methods start with some interpolation of the geodetic data in data space [e.g., *Bennett et al.*, 2003; *Shen et al.*, 1996; *Shen-Tu et al.*, 1998, 1999; *Snay et al.*, 1996; *Ward*, 1998; *Wdowinsky et al.*, 2001]. These studies have tended to concentrate on either the details of relatively small regions, or on relatively low resolution broad-scale features. None of these previous investigations incorporated surface fault creep as part of their model parameterization, whereas fault creep at the surface exists [e.g., *Lyons et al.*, 2002].

0148-0227/05/2003JB002742$09.00

[4] In this paper we analyze an updated version of the southwestern U.S. crustal velocity data set of *Bennett et al.* [2003], with the aim of capturing both the broad-scale pattern of deformation, and the finer-scale details of the deformation field in a single self-consistent surface deformation model. From this data set, we estimate the horizontal velocity gradient field, as well as surface creep on all major faults using the inversion procedure proposed by *Spakman and Nyst* [2002]. In contrast to many previous methods, this method is based on the kinematics of incremental deformation in a model space formulation which utilizes the physical relation between observations and model parameters. The method incorporates no assumptions about the dynamics or rheology of the crust. It allows for densification of the model parameterization in areas of increased data density, and accounts for both plate-scale deformation patterns and small-scale displacement discontinuities associated with near-surface fault creep. This multiscale parameterization has the potential to determine whether strong jumps in relative velocities across faults signify creep on the faults [*King et al.*, 1994; *Nicholson et al.*, 1986] or, alternatively, strain accumulation on locked seismogenic faults [*Bennett et al.*, 1996; *King et al.*, 1994]. The incorporation of surface creep in a joint inversion with the velocity gradient field is a unique characteristic of this method. Since GPS data are surface observations, surface creep is an intrinsic part of the data. Models based on this joint inversion therefore offer at or near the Earth's surface a physically justifiable description of the actual deformation field.

[5] We evaluate the consistency of the contemporary strain rate field as obtained from our inversion with the longer-term strain rate field derived from seismic data and geological fault slip data. Furthermore, we propose a model of how the Southwestern U.S. Deformation Zone (SWUSDZ) accommodates the relative motion between the Pacific and North American plates. We will also derive the moment deficit owing to the difference between the geodetic moment derived from our strain rate field and the seismic moment derived from moment tensor summation (restricted to the seismicity within the model area during the time span of observation). This analysis illuminates areas where the total deficit accumulation in the past 27 years has been of such an extent that a large earthquake could occur in the near future.

2. Tectonic Setting

[6] In the southwestern United States the boundary between the Pacific and North American plates is distributed across a 300–1000 km wide zone ranging from the Pacific coast to the state of Utah (Figure 1). The relative plate motion across the deformation zone amounts to ~50 mm yr^{-1} [*DeMets et al.*, 1990, 1994], of which only about 70% is accommodated by the San Andreas fault [e.g., *WGCEP*, 1995]. South of latitude 34°N, the remaining relative plate motion is distributed along neighboring parallel faults, such as the San Jacinto and Elsinore faults which all lie to the west of the San Andreas [*WGCEP*, 1995]. North of 34°N, the faults of the eastern California shear zone and Basin and Range province, east of the San Andreas system, also accommodate a significant fraction of the total plate motion. At 34°N the San Andreas fault changes its orientation from N40°W to N73°W due to a 160 km "left step" in the fault. It is generally accepted that this Big Bend section of the fault zone comprises a structural impediment to the plate motion [*Eberhart-Phillips et al.*, 1990] causing horizontal crustal shortening and vertical crustal thickening within the Transverse Ranges [*Argus et al.*, 1999]. The Santa Monica, San Gabriel, San Bernadino and Pinto Mountains can all be regarded as surface expressions of this convergence. North of the Big Bend, the San Andreas fault resumes an orientation almost parallel to the plate motion (N40°W). Farther north, around the latitude of 36.5°N the greater San Andreas system broadens, to include the Calaveras and Hayward faults, in addition to the San Andreas fault senso stricto.

[7] North of latitude 34°N, east of the greater San Andreas fault system, approximately 20–25% of the relative plate motion is transferred from the Salton Trough through the Mojave Desert via the eastern Californian shear zone (ECSZ) [*Dixon et al.*, 1995, 2000b; *Dokka and Travis*, 1990; *Gan et al.*, 2000; *Miller et al.*, 2001; *Sauber et al.*, 1994; *Savage et al.*, 1990]. The ECSZ inlet feeds the western Great Basin strain province [*Bennett et al.*, 2003], which encompasses both the geologically classified Walker Lane Belt (WLB) and the seismologically defined central Nevada seismic belt (Figure 1). At Mono Lake (~37.5°N), there is a broadening of the ECSZ deformation into the central and northern Walker Lane Belt (WLB) and the central Nevada seismic zone (CNSZ) located in the western Great Basin of the Basin and Range province [*Bennett et al.*, 2003; *Dokka and Travis*, 1990; *Oldow et al.*, 2001; *Savage et al.*, 1990, 1995] (Figure 1).

[8] West of this inboard shear zone, the central and eastern Great Basin provinces are characterized by a series of roughly north trending basin bounding normal faults [*Stewart*, 1971]. In contrast to the rather uniform distribution of faults, historical seismicity is primarily restricted to a narrow belt generally coincident with the greater Wasatch fault zone, called the intermountain seismic belt (IMSB). Contemporary crustal extension in this part of the Basin and Range province is distributed across a wide region that includes, but is significantly broader than, the intermountain seismic belt [e.g., *Bennett et al.*, 2003; *Friedrich et al.*, 2003].

3. Relative Motion Data

[9] Figure 2 shows the horizontal velocity estimates that comprise the data for this study. This data set is derived from a combination of velocity estimates from continuous networks (BARD, BARGEN, Eastern Basin-Range and Yellowstone Hotspot GPS Network (EBRY) (http://www.mines.utah.edu/rbsmith/RESEARCH/UUGPS.html), PGGA/SCIGN, and IGS) as well as from campaign data (SCEC [*Shen et al.*, 1996], northern Basin and Range province [*Thatcher et al.*, 1999], ECSZ [*Bennett et al.*, 1997; *Gan et al.*, 2000; *Miller et al.*, 2001], the Sierra Nevada [*Dixon et al.*, 2000b] and northeast Baja, California [*Dixon et al.*, 2000a]). The merging of these data sets is described by *Bennett et al.* [2002, 2003]. All velocity vectors in the combined solution refer to a common North America fixed reference frame. For our study we limit the data set to GPS and VLBI observation sites, which amounts to 497 stations located in the southwestern

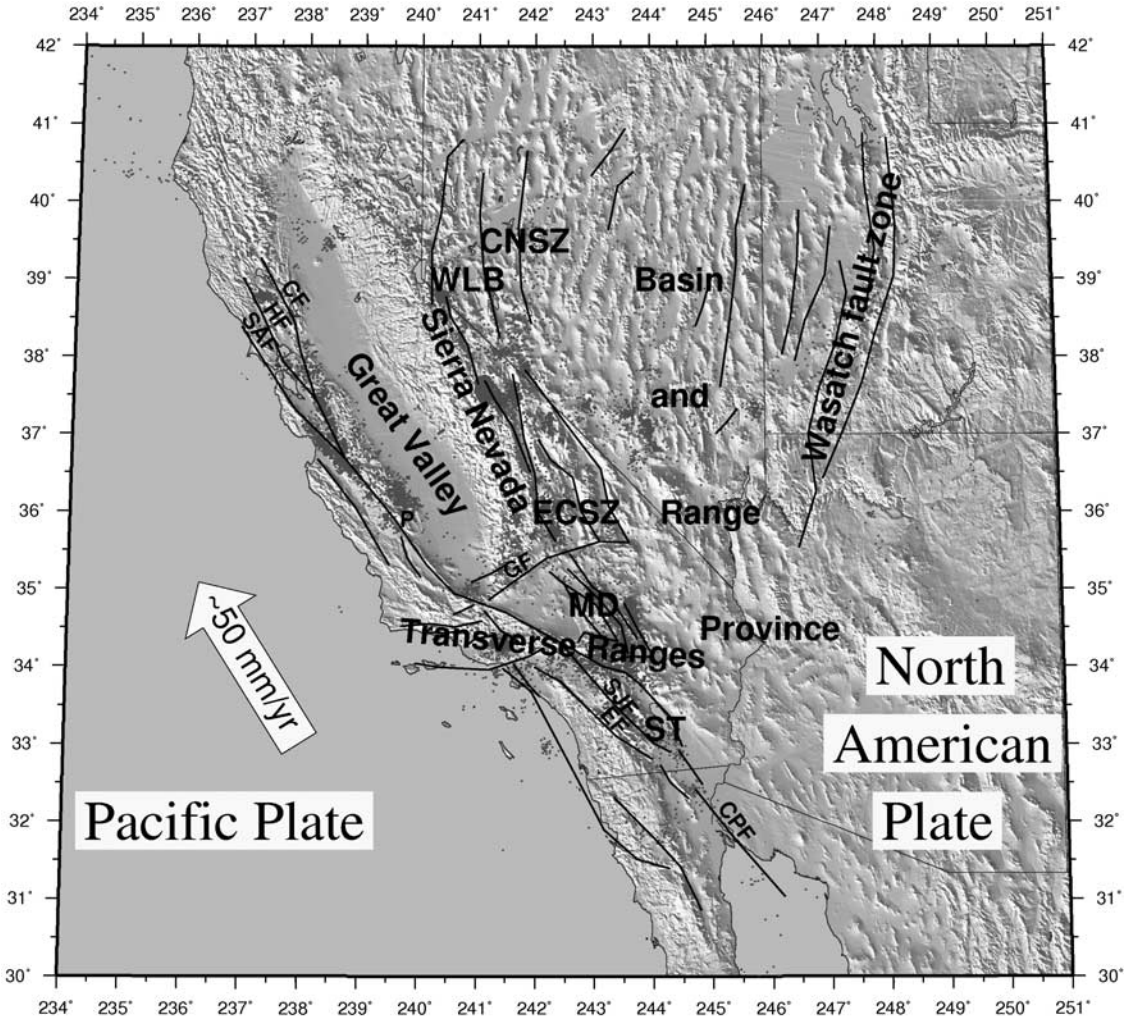

Figure 1. Tectonic setting of the southwestern U.S. deformation zone plotted against shaded relief illuminated from the west. Black lines indicate the fault traces utilized in our model parameterization. Orange dots indicate the shallow (<20 km) relocated seismicity of *Engdahl et al.* [1998]. MD, Mojave Desert; ST, Salton Trough; ECSZ, eastern California shear zone; CNSZ, central Nevada seismic zone; WLB, Walker Lane belt; SAF, San Andreas fault; HF, Hayward fault; CF, Calaveras fault; GF, Garlock fault; SJF, San Jacinto fault; EF, Elsinore fault; CPF, Cerro Prieto fault; P, Parkfield. See color version of this figure in the HTML.

United States, of which 194 are continuously operating GPS stations. The velocity estimates at the latter are in most cases significantly more precise than the campaign estimates. We do not consider those stations for which the 1σ velocity estimate uncertainties exceed 10 mm yr^{-1}. Fifty-seven stations in the combined data set are included in several of the campaign networks and/or a continuous GPS network. For these stations we either retain the velocity estimate derived from continuous GPS or the most precise estimate of relative motion for each station. At two stations in the Mojave Desert postseismic relaxation due to the Landers earthquake could be identified [*Shen et al.*, 1996]. Since our objective is to model the long-term, more stationary surface deformation field, we retain the pre-Landers velocity estimates.

4. Inversion Method and Model Parameterization

[10] We use the method of *Spakman and Nyst* [2002] to invert the relative motion data for estimates of the surface velocity gradient field (strain and rotation rate), and slip rate (creep rate) on major faults. In brief, the method utilizes the following observation equation for the relative motion Δv_{ij} between any two stations i and j:

$$\Delta \mathbf{v}_{ij} = \sum_{l=1}^{K+1} \int_{L_{ij}^{l}} \nabla \mathbf{v}(\mathbf{r}) \cdot d\mathbf{r} + \sum_{k=1}^{K} \alpha_k \mathbf{f}_k \left(r_{ij}^{k} \right) \qquad (1)$$

where

$$\nabla \mathbf{v}(\mathbf{r}) = \begin{bmatrix} v_{\phi\phi} & v_{\phi\theta} \\ v_{\theta\phi} & v_{\theta\theta} \end{bmatrix}$$

is the unknown velocity gradient field (with, e.g., $v_{\theta\phi}$ we indicate the rate of change of v_θ component with the ϕ coordinate in a spherical coordinate frame), $\mathbf{f}_k$ is the unknown fault slip rate (surface creep rate) on fault segment

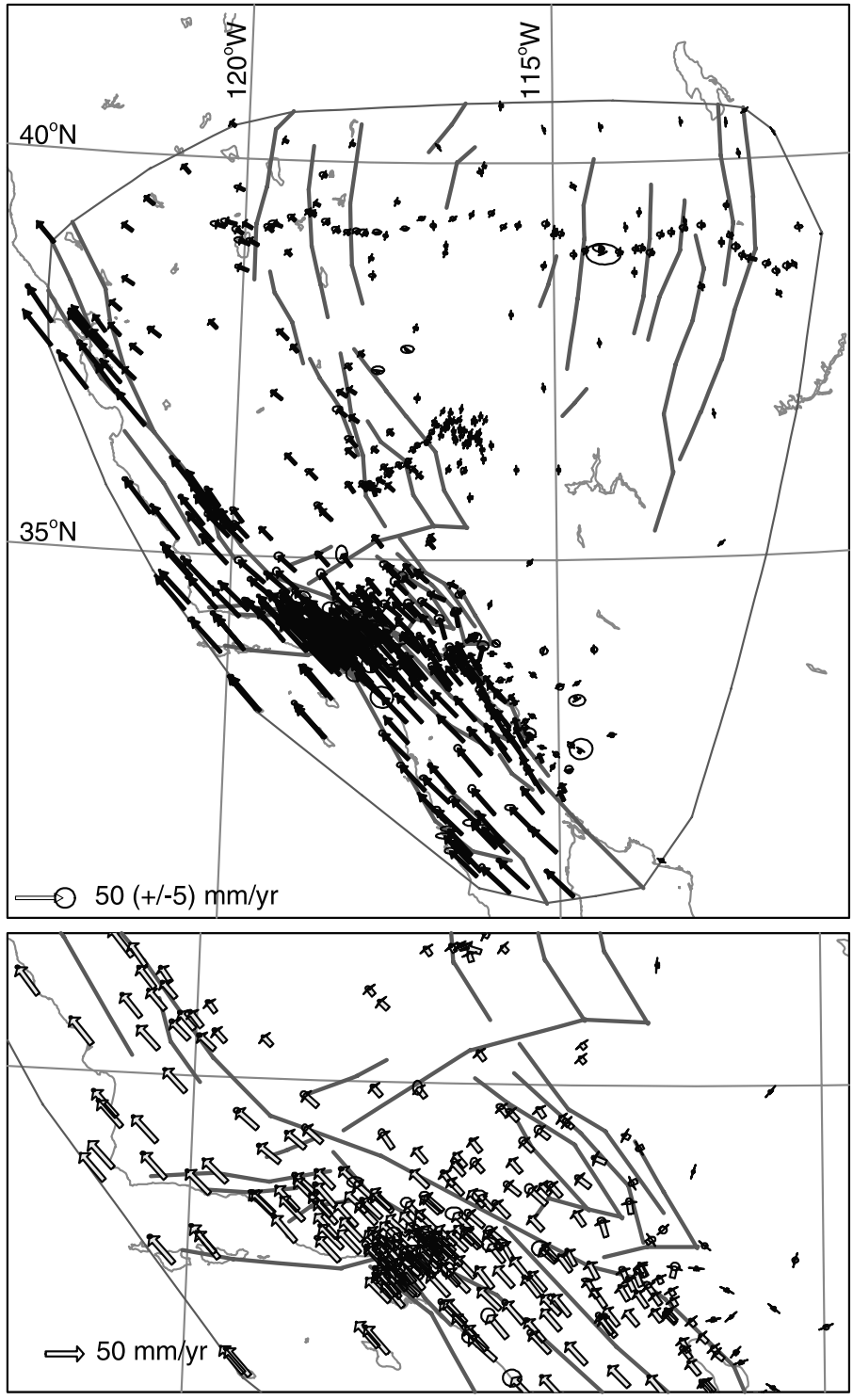

Figure 2. (top) Data set of 497 velocity vectors and their 95% confidence ellipses as utilized in this study. (bottom) Detailed view of southern California. Since the data density in southern California is very high, the station positions are also given in Figure 3.

k and $\alpha_k = +1$ or -1, depending on the fault orientation with respect to the direction of integration along path L. Any two stations are connected by a path L of arbitrary geometry (but usually the great circle) which is cut into segments at the locations (r_{ij}^k) where it crosses a fault leading to path segments L_{ij}^l. At these locations a fault slip term is added to account for the possible contribution of fault motion to Δv_{ij}. Equation (1) is exact in practice (the theoretical error in the right-hand side of (1) is much smaller than the error in $\Delta \mathbf{v}_{ij}$ [*Spakman and Nyst*, 2002]) and does not involve any knowledge of crustal rheology. The velocity gradient field is parameterized by assuming linear variation of its compo-

nents in triangular domains. A study region is subdivided by (spherical) triangulation using support points which become the model nodes. The spatial density of nodes can be varied to adapt to the local data density. Nodes need not coincide with station positions and triangle sides never cross faults. With this parameterization the model parameters are the components of the velocity gradient tensor at the model nodes. Fault slip rate (or creep rate) is parameterized by assuming constant slip rate on fault segments.

[11] Substitution of the model parameterization in (1) leads to a linear system of equations represented here by $\hat{\mathbf{A}}\mathbf{m} = \hat{\mathbf{d}}$, where $\hat{\mathbf{A}}$ is the observation matrix, $\mathbf{m}$ represents the collection of all model parameters, and $\hat{\mathbf{d}}$ is the vector of all combinations of relative motion between station pairs. The length of $\hat{\mathbf{d}}$ is of the order of $M(M-1)$ relative motion components where M is the number of stations. This set of equations can be extended by defining extra integration paths L between all station pairs. These extra paths are used to assure internal consistency between the velocity gradient field and fault motion/creep in constituting the total deformation field. A next set of equations derives from the fact that $\nabla \times \nabla \mathbf{v} = \mathbf{0}$ within regions bounded by faults. This constraint is defined for each single triangle leading to the linear equation $\alpha_r \mathbf{G}\mathbf{m} = \mathbf{0}$ where α_r is a weight used to tune the relative importance of these equations in determining a solution.

[12] The data equations and the curl constraints can be merged in one matrix equation $\mathbf{A}\mathbf{m} = \mathbf{d}$ which is solved by regularized least squares. The regularization is performed by extending $\mathbf{A}\mathbf{m} = \mathbf{d}$ with three sets of damping equations: (1) $\alpha_b \mathbf{I}\mathbf{m} = \mathbf{0}$ for damping the amplitude of $\nabla \mathbf{v}$ components on model's boundary nodes, (2) $\alpha_i \mathbf{I}\mathbf{m} = \mathbf{0}$ for spatially variable amplitude damping in nodes of the model interior, and (3) $\alpha_d \mathbf{D_2}\mathbf{m} = \mathbf{0}$ for penalizing the second derivative of the components of $\nabla \mathbf{v}$, where $\mathbf{I}$ is the identity matrix and $\mathbf{D}_2$ a second derivative operator (or discrete Laplacian smoother [*Segall and Harris*, 1987]). The amplitude damping assures a complete regularization of the extended matrix and avoids unwarranted amplitude excursions in regions of poor spatial resolution while the second derivative damping has a smoothing effect on the solution. For our application it proved unnecessary to damp the fault slip rate parameters.

[13] The formal least squares solution of the regularized system is:

$$\mathbf{m} = \left(\mathbf{A}^T\mathbf{C}_d^{-1}\mathbf{A} + \alpha_b^2\mathbf{I}_0 + \alpha_i^2\mathbf{I}_1 + \alpha_d^2\mathbf{D}_2^T\mathbf{D}_2\right)^{-1}\mathbf{A}^T\mathbf{C}_d^{-1}\hat{\mathbf{d}} \qquad (2)$$

which depends on the tuning of α_r, and the three regularization factors. The a posteriori model covariance is given by $\mathbf{C} = (\mathbf{A}^T\mathbf{C}_d^{-1}\mathbf{A} + \alpha_b^2\mathbf{I}_0 + \alpha_i^2\mathbf{I}_1 + \alpha_d^2\mathbf{D}_2^T\mathbf{D}_2)^{-1}$ and the model resolution kernel is $\mathbf{R} = \mathbf{C}\mathbf{A}^T\mathbf{C}_d^{-1}\mathbf{A}$.

[14] In our application M = 497 which leads to 123,256 integration paths taken along great circles. In total 246,512 alternative integration paths were added. The curl constraints amount to 1327 equations; thus in total we have 371,095 data equations. Inversion of the corresponding data covariance matrix is not feasible owing to its size. Instead we take for $\mathbf{C}_d$ a diagonal matrix with elements $\mathrm{Var}(\Delta v_{ij})_\phi \approx (\sigma_i)_\phi^2 + (\sigma_j)_\phi^2$ as an estimate of the variance for the velocity difference $(\Delta v_{ij})_\phi$ in longitudinal direction, where $(\sigma_i)_\phi$ and $(\sigma_j)_\phi$ are the data uncertainties for the stations i and j in longitudinal direction (and similarly in latitudinal direction).

[15] The model region is parameterized with 1327 triangles (Figure 3). The local density of GPS stations was used to guide densification in the triangulation. The triangles are spanned by 777 model nodes leading to 4×777 velocity gradient tensor components to be solved for. The major system of surface-breaking active faults in California and the Wasatsch fault zone were adopted from the U.S. Geological Survey (USGS). The Basin and Range province is characterized by diffuse fault zones which we mimic by a few single faults (Figure 3). In total we have 46 large fault traces. These are divided into 292 segments leading to 2*292 slip rate components in the model. The total number of model parameters is 3692 which defines the size of the matrix to be inverted to obtain the model $\mathbf{m}$ (equation (2)).

5. Inversion

[16] We have inverted the data for two different representations of the Southwestern U.S. Deformation Zone (SWUSDZ) crustal deformation field: the first (model I) is obtained by ignoring surface fault creep and represents the surface velocity gradient field assuming all faults in the region are locked at the surface, whereas the second (model II) allows for the presence of near-surface creep as well as continuous deformation. A comparison of these two models demonstrates how fault creep may affect the near-surface velocity gradient field.

[17] In order to quantitatively compare the two representations of crustal deformation we determine one set of regularization parameters for all models. For tuning of the covariance factor σ_r for the extra $\nabla \times \nabla \mathbf{v} = \mathbf{0}$ constraints and of the regularization parameters α_b, α_i, and α_d, we primarily focus on obtaining models (for inversions I and II, respectively) that are comparably resolved and obtain an acceptable model covariance. The spatial variation of the amplitude regularization (α_i) depends on the number of paths (hit count) contributing to each node; nodes with less hits than 1/8 of the maximum hit count were subjected to an increased regularization (α_{i_b}) with respect to the other nodes (α_{i_a}). Table 1 shows the regularization parameters used to obtain our model solutions.

[18] The normalized data misfit values χ^2 per degree of freedom [*Bos et al.*, 2003] provide a measure of how well the models can fit the data (Table 1). On the basis of a 1σ data error model II provides the best data fit, however, none of the models can fit all local variations in the velocity data within the 1σ data standard deviation. On a 95% confidence level, both models fit the data within the standard deviations ($\chi_I^2 = 0.87$ and $\chi_{II}^2 = 0.66$).

[19] Figures 4 and 5 show the 3σ model standard deviations of all four components of the velocity gradient and the diagonal elements of the resolution matrix (R_{ii}) of the $v_{\phi\phi}$ and $v_{\theta\theta}$ components of the velocity gradient tensor of models I and II, respectively. Standard deviations exceeding 100% of the model value have not been contoured. These occur mostly in regions that have obtained small amplitudes in the velocity gradient components. The R_{ii} values for $v_{\phi\theta}$ and $v_{\theta\phi}$ are comparable to the values of $v_{\phi\phi}$ and $v_{\theta\theta}$, respectively. Since part of the data signal in model II is

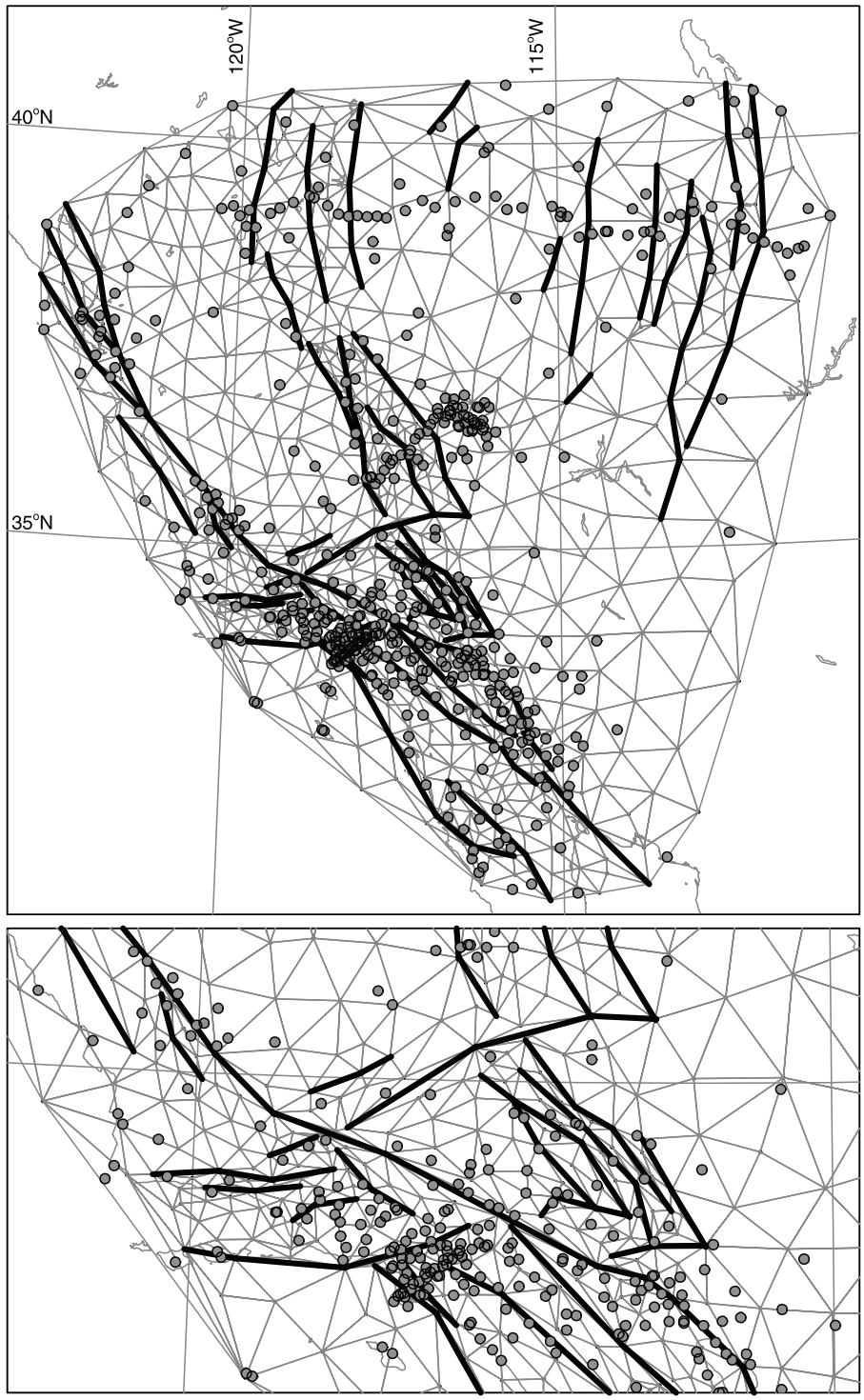

Figure 3. (top) Final parameterization of the SWUSDZ models. (bottom) Detailed view of southern California. Thick lines indicate fault segments, solid dots are the triangle nodes, and grey dots are the site positions. Note that in our choice for the triangle nodes we are not restricted to the locations of the observation sites. Triangles do not intersect faults. Nodes at the fault are doubled to allow the velocity gradient field to be discontinuous across faults.

explained by motion on faults, larger areas now render velocity gradient values not significantly different from 0 in either or both directions. The 3σ errors on the surface fault creep of model II do not exceed 0.9 mm yr^{-1}. Generally, we observe a strong reduction in resolution along the model boundary, consistent with the increased damping of the model on the boundary. We also observe a reduction of resolution around some of the faults in model II, indicating a trade-off between the fault motion components and the velocity gradient components.

Table 1. Aspects of the Inversion Parameterization and Average Results for Inversions I and II[a]

Model	σ_r, 10^{-7} m yr^{-1}	α_b, 10^9	α_{i_a}, 10^8	α_{i_b}, 10^8	α_d, 10^8	χ^2	$\tilde{r}_m$	$\tilde{\sigma}^c_m$, 10^{-9} yr^{-1}	$\tilde{\sigma}^f_m$, mm yr^{-1}
Velocity gradient field	3.5	3.0	2.0	4.0	3.0	5.27	0.66	1.20	-
Joint solution	3.5	3.0	2.0	4.0	3.0	3.98	0.66	1.36	0.049

[a]Explanations are as follows: σ_r, standard deviation of the $\nabla \times \nabla \mathbf{v} = \mathbf{0}$ equations; α_b, α_{i_a}, α_{i_b}, and α_d, the regularization parameters; T_n, number of model nodes; K, number of fault segments; $\tilde{r}_m = (1/M)\sum_{i=1}^{M} R_{ii}$, the average resolution, with R_{ii} the diagonal elements of the resolution matrix and M the number of model parameters; $\tilde{\sigma}^c_m = (1/M_c)\sum_{i=1}^{M_c} \sqrt{C_{ii}}$, the average standard deviation for the components of $\nabla \mathbf{v}$, with $M_c = 4T_n$ the number of components of $\nabla \mathbf{v}$; $\tilde{\sigma}^f_m = (1/M_f)\sum_{i=1}^{M_f} \sqrt{C_{ii}}$, the average standard deviation for the components of $\mathbf{f_k}$, with $M_f = 2K$ the number of slip components.

[20] From their synthetic tests, *Spakman and Nyst* [2002] inferred that a basic trade-off between the fault creep rates and the velocity gradient field may exist in the joint analysis. This trade-off is a direct result of the lack of physical constraints that couple fault motion to continuous deformation in a purely kinematic inversion of relative motion data. The trade-off is best resolved when relative motion observations exist close to the fault zones. If this is not the case, the surface creep rates obtained from data inversion may in part reflect block rotations.

[21] However, recently, *Bos et al.* [2003] demonstrated the importance of incorporating fault creep in our inversion. For the almost freely slipping Longitudinal Valley Fault (LVF) of Taiwan, our joint inversion of the dense GPS data set across the fault, resulted in a well resolved fault creep rate of 20–25 mm yr^{-1}. This is consistent with creep rate measurements along the fault. The velocity gradient field in this joint solution differed significantly from that obtained in the locked fault solution and resulted in a novel interpretation of the surface deformation field at Taiwan.

[22] Since surface creep rates have also been identified for the southwestern United States [*King et al.*, 1994; *Lienkaemper et al.*, 1991; *Lyons et al.*, 2002; *Lyons and Sandwell*, 2003; *Nicholson et al.*, 1986; *Rosen et al.*, 1998; *Schulz et al.*, 1982; J. Langbein, Parkfield creep meter data: Detrended measurements from the past 10 years, 2002, available at http://quake.wr.usgs.gov/QUAKES/geodetic/twocolor/creep_pkf_10yr_det.gif] model II is a viable alternative to explain the data of this region. Careful comparison of the modeled creep rates to the observed rates (appendix in the auxiliary material[1]) in conjunction with a close inspection of the data density across the faults allows for an analysis of the trade-off problem and enables a proper interpretation of model II.

6. Model Description

6.1. Fault Motion

[23] A quantitative comparison of the surface creep rates of model II (Figure 6) to geological slip rates, as well as creep measurements (section A of the appendix in the auxiliary material) shows a general agreement for the sense of motion on the faults. In regions with dense station coverage in the vicinity of the faults, where the spatial resolution is high, we model significant aseismic surface creep (section A of the appendix in the auxiliary material).

[24] The solution shows relatively large surface creep (8–35 mm yr^{-1}) on the San Andreas, Calaveras, Concord/Green Valley (San Francisco Bay (SFB)), Paicines (SFB), Imperial Valley, and Cerro Prieto faults. Significant surface creep (2–8 mm yr^{-1}) is also observed on the San Jacinto, Elsinore, Laguna Salada, San Juan, San Miguel, San Pedro Matir, Hayward, Rogers Creek (SFB), Headsburg (SFB) and Camp Rock (Mojave Desert) faults (section A of the appendix in the auxiliary material). In model II, the Californian shear zone is dominated by dextral motion. In the Transverse Ranges significant thrusting is observed. This thrusting is accompanied by dextral slip on the Santa Ynez fault (~1 mm yr^{-1}; WTR), Big Pine fault (~0.4 mm yr^{-1}; WTR) and Pinto Mountain fault (~2 mm yr^{-1}; eastern Transverse Ranges (ETR)). The model obtains a combination of normal faulting and dextral slip in the eastern Californian shear zone (ECSZ), Walker Lane Belt and the central Nevada seismic zone (CNSZ). Sinistral thrust motion (~2 mm yr^{-1}) is obtained on the Wasatch fault zone.

6.2. Strain and Rotation Rate

[25] Both models I and II show a clear Californian shear system (Figure 7). In the shear zone, variations in contractional and extensional patterns in the effective strain rate do not indicate a change in dominant regime, but a small dominance of either principal strain rate. In model II the magnitude of the strain rates within the California shear zone has been reduced due to the presence of fault creep. The principal axes show a rotation along with the change of orientation of the San Andreas fault in the Big Bend of the fault. In the ECSZ the dextral normal motion on the faults significantly reduces the extension observed in model I and changes the orientation slightly from WNW-ESE to pure E-W. Both models show a distinct asymmetry of the deformation at the San Andreas fault in central California, between the Big Bend section and San Francisco. The deformation tends to concentrate on the eastern side of the San Andreas fault, in the Great Valley (Figure 7). The deformation becomes much more diffuse and spatially distributed across the Transverse Ranges. In southern California it mainly localizes between the San Jacinto and San Andreas faults, especially in model II (Figure 7).

[26] Many regional aspects of the deformation of model I compare well with those obtained in earlier studies based on geodetic data and ignoring active fault motion (section B of the appendix in the auxiliary material). It is difficult to indicate the extent to which the discrepancies result from differences in methodology between the various approaches and different data sets used. We note however that significant differences between these earlier studies and model II exist and that these are a direct result of the implementation of fault creep in our methodology. Further, we deduce that despite retaining the pre-Landers observations, postseismic relaxation of the Landers earthquake affects our surface

[1]Auxiliary material is available at ftp://ftp.agu.org/apend/jb/2003JB002742.

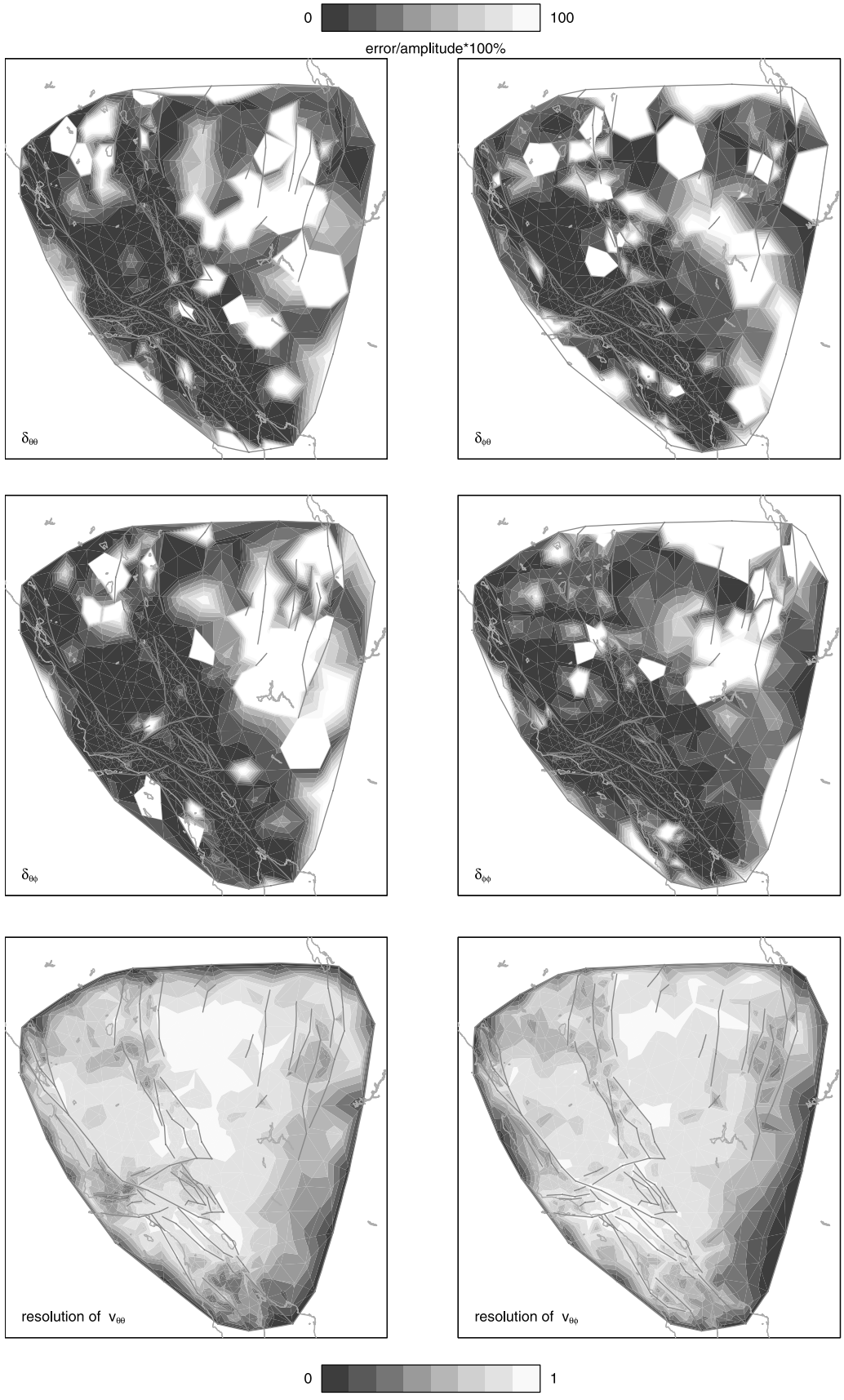

Figure 4. Model standard deviations corresponding to a 95% confidence level and resolution of model I. The model standard deviations are expressed as percentage of the component magnitude.

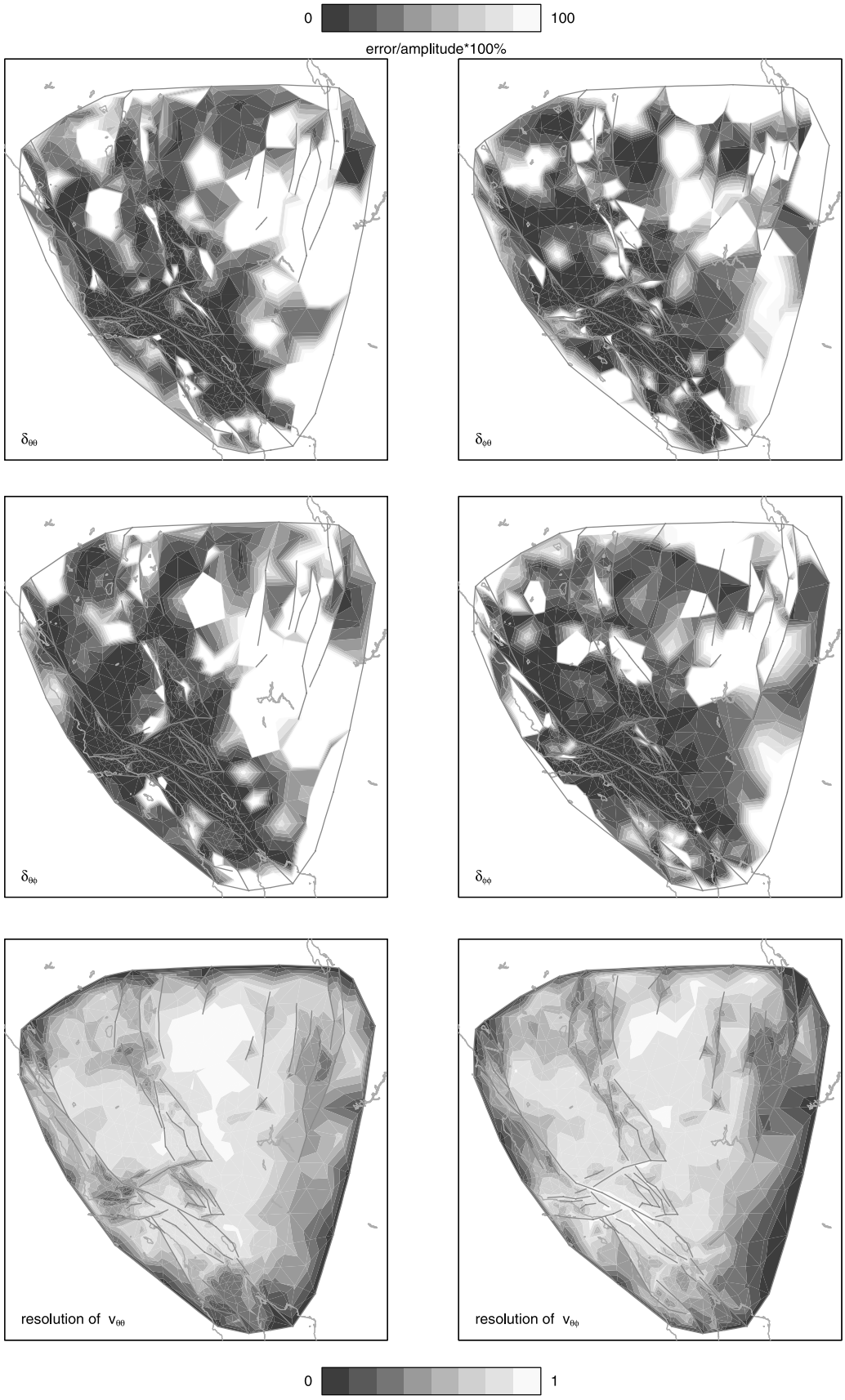

Figure 5. Model standard deviations and resolution of model II.

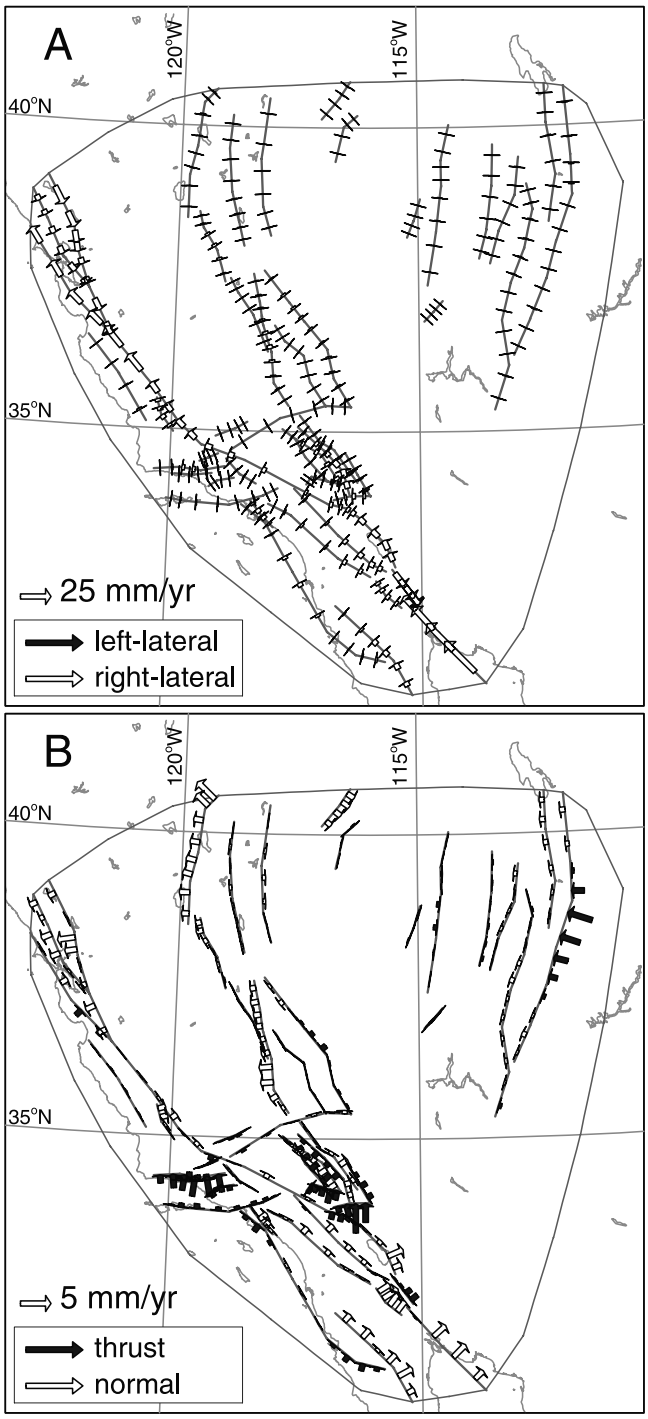

Figure 6. Fault motion contribution of model II. (a) Lateral component of the fault motions; (b) perpendicular component of the fault motions. Note the different scales of the slip vectors.

deformation field, while the postseismic relaxation related to the Northridge and Loma Prieta earthquakes have no influence on our models (section C of the appendix in the auxiliary material). However, postseismic relaxation of several other earthquakes may possibly affect our models in the ECSZ, the western Transverse Ranges, along the Parkfield segment of the San Andreas fault and at Salton Trough. We are presently unable (due to lack of data) to quantify the extent of their influence on our surface deformation models. We further note that significant seismicity, as well as postseismic linear elastic relaxation is present in

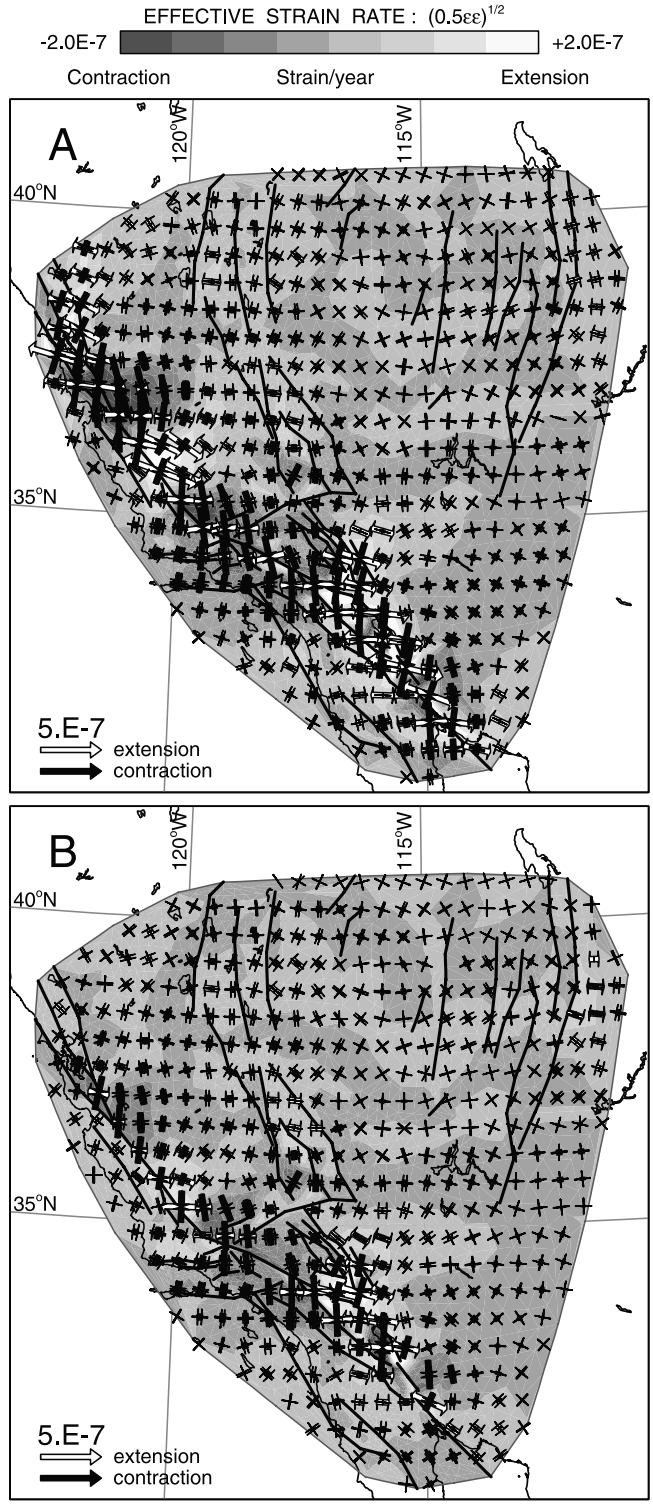

Figure 7. Strain rate contribution of (a) model I and (b) model II. The arrows denote the principal strain rates: contraction (red) and extension (blue). See color version of this figure in the HTML.

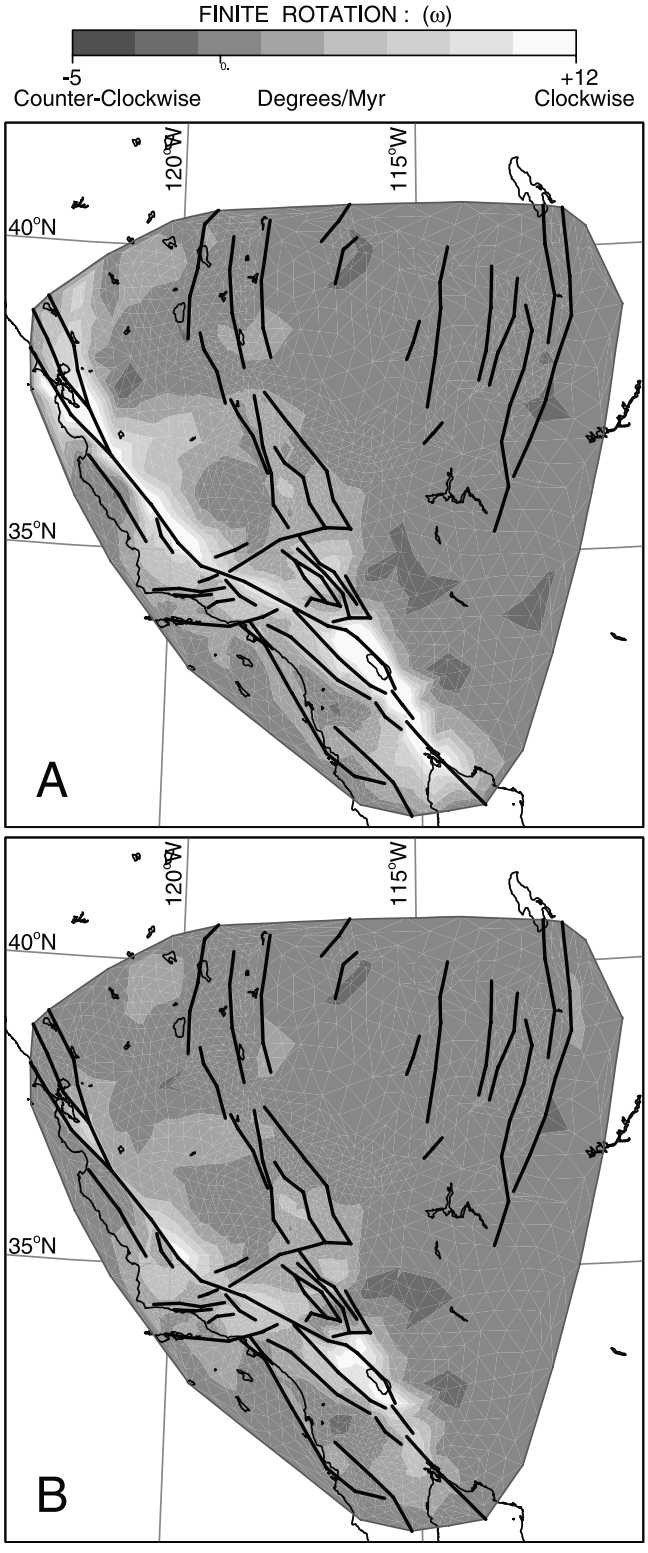

Figure 8. Rotation rate contribution of (a) model I and (b) model II. Note the location of the zero in the contour scale. See color version of this figure in the HTML.

the model area and may locally be incorporated in our models.

[27] Both models I and II show strong clockwise rotations along the San Andreas fault, Mojave Desert, ECSZ, CNSZ and Walker Lane Belt, consistent with dextral shear (Figure 8). We notice an asymmetry of the rotations with respect to the faults along the Parkfield and Carrizo segments of the San Andreas fault. Model II shows minor counterclockwise rotation of $1-2^\circ$ Myr^{-1} in the southern Mojave Desert.

[28] Strain rates in the Basin and Range are almost an order of magnitude smaller than those observed in the shear zone. The deformation in the Basin and Range province appears to be dominated by north-south variations in the principal axes orientations. East of the Wasatch fault zone significant E-W extension is obtained in both models, whereas the western Basin and Range shows extension-dominated right-lateral shear. Although the spatial distribution of deformation in the Basin and Range remains debated, general consensus exists on the fact that it is dominated by NW-SE extension [*Bennett et al.*, 1999, 2002; *Flesch et al.*, 2000; *King et al.*, 1994; *Lachenbruch et al.*, 1994; *Thatcher et al.*, 1999]. In the Basin and Range the data density is rather low. The data are concentrated along three more or less east-west orientated transects of which the central transect is very densely sampled owing to the *Thatcher et al.* [1999] campaign data set. Compared to this transect, the distribution of the Continuous GPS network stations in the Basin and Range is sparse. Although the campaign data are of lower precision, they dominate the regional estimation of the velocity gradient field. We found that a sinusoidal pattern in the N-S component of the campaign data set of *Thatcher et al.* [1999] dominates the deformation patterns obtained in the Basin and Range province (see section D of the appendix in the auxiliary material for a detailed analysis). This data set is also responsible for the large extension east of the Wasatch fault zone observed in our model (see section D of the appendix in the auxiliary material).

6.3. Asymmetry of the Surface Deformation Field

[29] Though in central California, north of the Big Bend, deformation concentrates at the San Andreas fault, both models I and II show a distinct asymmetry of the strain and rotation rates across the fault (Figures 7 and 8). The deformation localizes on the eastern side of the fault. The asymmetry in the strain rate field across the San Andreas fault extends over several triangles and is well resolved (Figure 5) (i.e., the projection of actual surface deformation on our model basis functions (parameterization) is well resolved).

[30] Figure 1 shows an updated version of the relocated seismicity data of *Engdahl et al.* [1998] in the southwestern United States. Most of the seismicity occurs at or close to the major faults. However, there is significant seismicity east of the San Andreas fault in the Great Valley, which correlates with high strain rates in our deformation field. Though this seismicity may be related to the presence of blind thrust faults east of the San Andreas fault (USGS fault data set, *Unruh and Lettis* [1998], and the 1983 Coalinga earthquake), our velocity gradient field shows shear-dominated strain rates along the San Andreas fault in this area.

[31] Previous surface deformation studies have not obtained this asymmetry possibly due to coarser/smoother model parameterization [*Shen-Tu et al.*, 1998; *Ward*, 1998] or the asymmetry was not addressed [*Jackson et al.*, 1997; *Shen-Tu et al.*, 1999]. However, when studying displace-

ment data caused by the 1906 San Francisco event, *Chinnery* [1970] found an asymmetry in the data across the San Andreas fault in the vicinity of Fort Ross. *Huggett et al.* [1977] obtained measurements of strain from multi-wavelength distance-measuring (MWDM) observations near Hollister. They observed large strains occurring away from and only on one side of the San Andreas and Calaveras faults and postulated that this may have been caused by movement of one side of the fault.

[32] *Malservisi et al.* [2001] related an asymmetric surface deformation field in the ECSZ to a viscosity contrast. The viscosity contrast relates to differences in heat flow, where strain localizes in high heat flow regions. However, this cannot explain the asymmetry across the San Andreas fault since no heat flow contrast is observed across the fault [*Sass et al.*, 1994, Figure 1]. *Mahrer and Nur* [1979] and *Rybicki* [1978] determined displacement fields for static two-dimensional models of a long strike-slip fault in a crust of laterally varying rigidity. They observe a significant reduction of displacement on the high-rigidity side of the fault, as well as a shift of the peak displacement toward the fault trace on both sides. Such a distinct rigidity contrast would also have important implications for the crustal velocity structure across the fault.

[33] *Healy and Peake* [1975] determined seismic velocity changes at Bear Valley. They observed velocity variations extending a number of km away from the fault trace and asymmetric across the fault. The same nonsymmetry was obtained by *Boore and Hill* [1973]. On the basis of this contrast they deduced that the rigidity east of the San Andreas fault is smaller than west of the fault by a factor of $\sim$1.7. Across the Parkfield segment of the San Andreas fault, *Eberhart-Phillips and Michael* [1993] obtained a 5–20% lateral change in velocity over 4 km width. By combining the velocity model with a resistivity model, they were able to deduce corresponding rock units. The high velocities to the southwest of the fault are inferred as high-resistivity basement of Salinian granite. The large volume of low-velocity, low-resistivity material northeast of the San Andreas fault is inferred to be overpressured Franciscan of Great Valley sequence material. Assuming that the stress level at both sides of the fault is comparable, (based on both models) we deduce a rigidity contrast across the fault of $\sim$1.78, consistent with *Boore and Hill* [1973]. Since the same velocity contrast across the fault is still prominent at Bear Valley, this crustal structure may extend all along the San Andreas fault from the Big Bend to the Calaveras junction, thus providing a feasible explanation for the localization of deformation east of the fault.

7. Crustal Deformation of the SWUSDZ

[34] *King et al.* [1994] derived that since 1850 about 60% of the Pacific-North American motion occurred seismically and 40% aseismically. They further showed that within the seismogenic depth range of the plate boundary aseismic deformation is concentrated near the surface and at depth. In some cases this deformation can be located on creeping faults, but elsewhere it is spread over a several kilometer wide zone adjacent to the fault. We infer that this kind of surface deformation field is clearly modeled in model II. On the basis of model II we derive a model of the kinematics of the present-day surface deformation of the SWUSDZ. Figure 9 summarizes the main features for strain, rotation and slip rates of our model.

[35] Within the shear zone of California we can identify many faults containing dextral motion and significant clockwise (CW) rotations. More in depth, we can distinguish several fault zones bounding rotating blocks. Around the San Francisco Bay, we obtain dextral creep on the San Andreas, Hayward and Calaveras fault system. The southern part of this system is associated with CW rotations and shear strain rates in a setting dominated by contraction. To the east of the San Andreas-Calaveras fault junction the model depicts significant shear strain rates also in a setting dominated by contraction possibly related to hidden thrusts in the area. The eastward extent of these shear strain rate patterns is poorly constrained by the lack of data within the Sierra Nevada. The Parkfield segment of the San Andreas fault (SAF) is dominated by asymmetric shear strains in a predominantly extensional setting, southward diminishing dextral creep and asymmetric CW rotations. Between the San Andreas-Calaveras fault junction and the Big Bend section of the San Andreas fault, deformation localizes on the eastern side of the San Andreas fault which we have attributed to a significant rigidity contrast across the fault. The Big Bend section marks the transition from N-S contraction in the western Transverse Ranges to dextral shear in the Mojave Desert. The Transverse Ranges are associated with sinistral creep and significant CW rotations. The southern Mojave Desert experiences counterclockwise rotations to accommodate the CW rotations in the eastern Transverse Ranges. The rotating blocks in the eastern Transverse Ranges and Mojave Desert are bounded by dextral faults. The ECSZ, Walker Lane Belt and CNSZ show a continuous shear zone of dextrally creeping faults separated by CW rotating blocks. In contrast to the Mojave Desert, the faults bounding the Sierra Nevada obtain a significant normal component of fault creep accommodating the extension of the Basin and Range. The White Mountains seismic gap between the ECSZ and the CNSZ is dominated by shear, thus transferring the deformation from the ECSZ to the CNSZ. The western Great Basin undergoes significant WNW-ESE extension. The San Andreas and San Jacinto faults are linked as a single dextral fault system. Between the two dextral faults significant CW rotation and dextral shear occurs consistent with deformation in a dextral fault zone. The southward extension of the San Andreas fault, the Imperial Valley fault and the Cerro Prieto fault also show significant dextral creep.

8. Moment Deficit Analysis

[36] Assuming a stationary strain rate field between 1973 and 2000, we determine the moment deficit field by calculating the difference between the geodetic moment accumulated during this period and the estimated seismic moment released during the same time interval. Analysis of this moment deficit field will allow for the identification of regions where the deficit accumulation during the 27 years of observation has been of such an extent that a large earthquake could occur in the near future.

[37] *Kostrov* [1974] codified the relationship between the strain rate tensor $\dot{\epsilon}$ and earthquake activity. In addressing

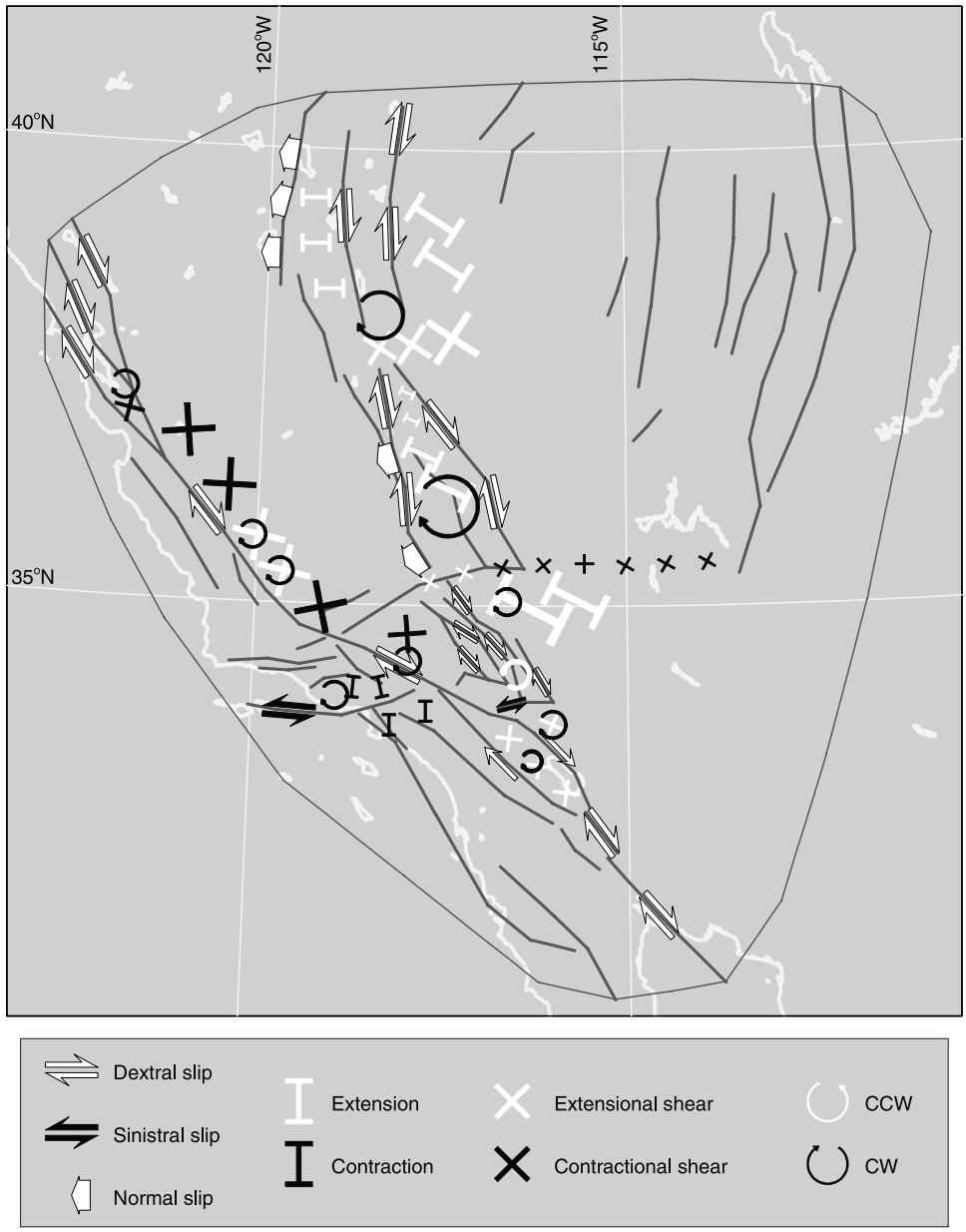

Figure 9. Model of the kinematics of the present-day surface deformation of the SWUSDZ. With extensional shear we indicate shear strains in which the magnitude of the extensional principal axes exceeds the contractional principal axes. With contractional shear we indicate shear strains for which the magnitude of the contractional axes exceeds the extensional axes.

earthquake moment rates we adopt the scalar version of this formula according to *Ward* [1998]:

$$\dot{\overline{M}} = 2\mu A H_s^A \dot{\bar{\epsilon}}_{\max}^A \tag{3}$$

where $\dot{\overline{M}}$ represents the mean earthquake moment rate for a seismogenic region with surface area A, $\dot{\bar{\epsilon}}_{\max}^A$ the averaged maximum strain rate of this region and $\mu = 3.0 \times 10^{10}\,\mathrm{N\,m^{-2}}$, the rigidity of the elastic layer. H_s^A in equation (3) is the average thickness over which elastic strains accumulate and dissipate in earthquakes. H_s^A is neither the crustal thickness nor the maximum depth of earthquakes. These depths exceed H_s^A because the top few kilometers of the crust behave aseismic and the properties of the deepest quakes do not reflect the seismogenic layer as a whole. *Ward* [1998] determined average values of H_s^A = 12.7 km for southern California, H_s^A = 11.2 km for northern California and H_s^A = 14.7 km for the Basin and Range. We have adopted these values in our analysis.

[38] In principle, most of our model area should be considered as seismogenic and a single mean moment rate may be determined (e.g. similar to the approach taken by *Ward* [1998]). We are more interested in the local accumulation of the moment deficit. We could adopt our triangular parameterization and determine a mean moment rate for each triangle. However, our triangle sizes are variable, and this will introduce a surface area dependence

into our moment deficit field. In order to avoid the influence of the varying triangle sizes on the mean moment rates, we construct a grid of square cells with $A = 0.25^\circ \times 0.25^\circ$ within our model area. For each grid cell we subsequently determine the total geodetic and the total seismic moment.

[39] We adopt the strain rate field of model I for the determination of the total geodetic moment that has accumulated during the 27 year observation period. Near-surface creep in model II relaxes the near-surface strain. This relaxation may in fact enhance the stresses on the deeper locked part of the fault. Thus the velocity gradient field of model II may not represent the deformation field of the seismogenic zone (where the faults are likely locked). In contrast, model I is based on the assumption that all faults are locked up to the surface. We assume that model I is a better representation of the deformation field in the seismogenic zone than model II. The average maximum strain rate of each cell is derived from the maximum strain rates in model I at the corners of the cell and the mean moment rate is determined using equation (3). By multiplying these moment rates with the time span covered by the data (1973–2000) we obtain the total accumulated (geodetic) moment of each grid cell.

[40] From the USGS seismicity database and the Harvard centroid moment tensor catalogue we can determine the seismic moment rate for each grid cell for the same period. For the events obtained from the USGS database we use the $M_0 - M_l$ relation of *Thatcher and Hanks* [1973] for southern California ($\log M_0 = 1.5M_l + 16.0$) to determine the seismic moment of these event. By applying moment summation on the seismic moments of all events located within a particular grid cell, we obtain the total seismic moment of the grid cell within the time span considered.

[41] The moment magnitude (M_w) of an earthquake is related to the seismic moment (M_0, given in dyn cm) by [*Kanamori*, 1977]

$$M_w = \left(\frac{\log M_0}{1.5}\right) - 10.73 \quad (4)$$

By replacing M_0 in equation (4) by the moment deficit (M) we determine the earthquake magnitude corresponding to each moment deficit (Figure 10). Thus the moment deficit accumulated or released during the period of observation is represented by a single earthquake within each grid cell with given moment magnitude.

[42] These moment magnitudes represent a minimum for an earthquake that could occur in a grid cell. Near known faults, we expect the earthquake to occur on a major fault or on (hidden) secondary faults. Remote from major faults the interpretation is less useful, unless the accumulated strain would be released on a new or hidden fault). From Figure 10 we can see larger earthquakes diminishing the moment deficit. The large events in the region (e.g., Landers, Hector Mine, Northridge and Loma Prieta) have released more seismic moment than was accumulated geodetically in this time period (negative magnitudes). Of course large earthquakes release seismic energy and moment across larger areas than just their epicenter. This more regional influence of the large events is not explicitly incorporated in our analysis, however, is taken into account in the

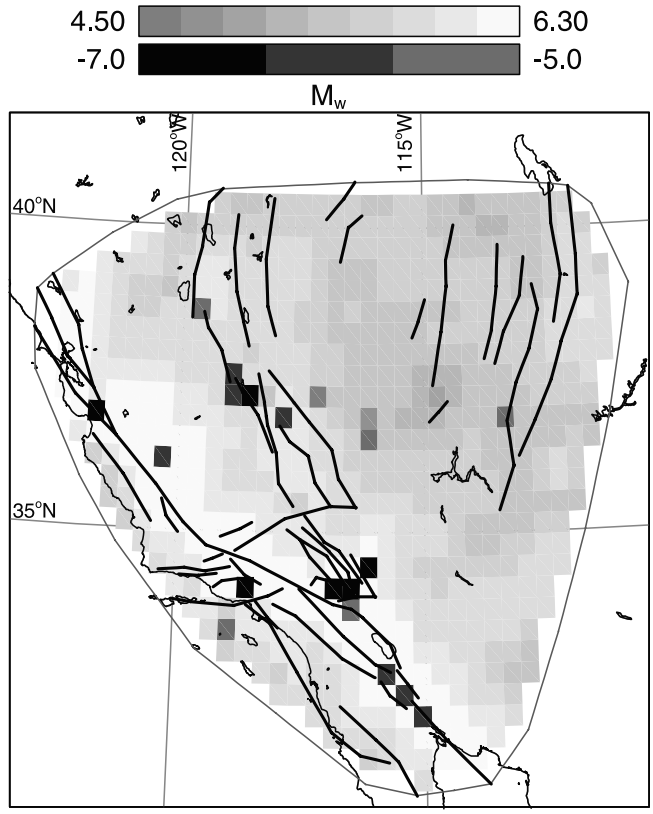

Figure 10. Moment magnitudes corresponding to the moment deficits accommodated in our model area during our observation period. The negative moment magnitudes correspond to negative moment deficits, indicating that large earthquakes within the observation period have released more seismic moment than has been accumulated by our strain rate field. See color version of this figure in the HTML.

interpretation of Figure 10. In the western Transverse Ranges, the Northridge earthquake and aftershocks have released most of the moment build up by the strain rates of our model within the time period, thus reducing the moment deficit in this area. The same holds for the Mojave Desert, where the Landers, Big Bear and Hector Mine earthquakes released a significant amount of the accumulated moment. However, all along the San Andreas fault we find moment deficits corresponding to $M_w > 5.9$. In southern California, away from the San Andreas fault, we find relatively low moment deficits corresponding to $M_w \sim 5.5$. Significant moment deficit, corresponding to $M_w = 6.1–6.3$, has accumulated east of the Parkfield and Carrizo segments of the San Andreas fault. A comparable moment deficit is also observed in the San Francisco Bay area, along the San Andreas fault just north of the Big Bend and around the Imperial and southern San Andreas faults. On the Hayward and southern Calaveras faults these high moment deficits coincide with regions of increased microseismicity. A similar increase of microseismicity has been observed prior to some significant events (e.g., the 17 August 1999, Izmit, Turkey, earthquake [*Nalbant et al.*, 1998; *Parsons et al.*, 2000]) and may thus point at an

increased risk of an earthquake to occur in these regions in the near future.

9. Conclusions

[43] We have estimated the surface deformation field of the southwestern U.S. deformation zone in terms of (1) the velocity gradient field and (2) the velocity gradient field and surface creep simultaneously.

[44] The two models we obtained provide an integral view on the deformation of the SWUSDZ which results from all driving forces (e.g., plate interaction, basal stresses). A comparison of the two models demonstrates that the velocity gradient field is very sensitive to whether or not fault creep occurs. Model II provides the best fit to the geodetic data. The model shows aseismic fault motion which sense of motion is generally in agreement with geological observations. In densely sampled areas, the fault motion is consistent with aseismic creep measurements. However, to some extent (depending on GPS observations close to the faults) a trade-off between fault motion and the velocity gradient field exists throughout our model. The surface deformation field shows distributed deformation in a zone around the faults with significant shear strain rates and rotations, though significant distributed deformation away from the faults is also observed. The eastern California shear zone acts as a distinct fault zone, bounded by more rigid blocks. The faults within the zone take up a significant part of the shear motion, while shear strain rates and clockwise rotations are located between the bounding faults. Similarly, the San Jacinto and San Andreas faults act as bounding faults of a fault zone with significant shear strain rates and clockwise rotations. The Mojave Desert is dominated by right-lateral shear, whereas the western Transverse Ranges show significant contraction. Significant localization of deformation east of the San Andreas fault is observed between the Big Bend section and the San Andreas-Calaveras fault junction. We explain this as a result of a significant rigidity contrast across the fault associated with a more rigid Salinian granite basement west of the fault and less rigid Franciscan or Great Valley sequence material east of the fault. In this area our moment deficit analysis shows an accumulation of moment deficit between 1973 and 2000 which corresponds to a $M_w = 6.1–6.3$ earthquake. Near the San Francisco Bay, along the San Andreas fault just north of the Big Bend and around the Imperial and southern San Andreas faults a comparable deficit has accumulated. On the Hayward and southern Calaveras faults the accumulation of moment deficit coincides with significant microseismicity. This may point at an increased risk of an earthquake occurring in these regions in the near future.

[45] **Acknowledgments.** We would like to thank Shimon Wdowinsky, John Beavan, and an anonymous reviewer for their valuable comments. We thank Rick Bennett for providing his unpublished data set. The model triangulation was made with a program by *Shewchuk* [1996]. This research was conducted under the research programs of the Vening Meinesz Research School of Geodynamics (VMSG) and the Netherlands Research Center for integrated Solid Earth Sciences (ISES).

References

Argus, D. F., M. B. Heflin, A. Donnellan, F. H. Webb, D. Dong, K. J. Hurst, D. C. Jefferson, G. A. Lyzenga, M. M. Watkins, and J. F. Zumberge (1999), Shortening and thickening of metropolitan Los Angeles measured and inferred by using geodesy, *Geology*, *27*(8), 703–706.

Bennett, R. A., W. Rodi, and R. E. Reilinger (1996), Global Positioning System constraints on fault slip rates in southern California and northern Baja, Mexico, *J. Geophys. Res.*, *101*, 21,943–21,960.

Bennett, R. A., B. P. Wernicke, J. L. Davis, P. Elosegui, J. K. Snow, M. J. Abolins, M. A. House, G. L. Stirewalt, and D. A. Ferrill (1997), Global Positioning System constraints on fault slip rates in the Death Valley region, California and Nevada, *Geophys. Res. Lett.*, *24*(23), 3073–3076.

Bennett, R. A., J. L. Davis, C. M. Meertens, R. B. Smith, and B. P. Wernicke (1998), Integration of the northern Basin and Range (NBAR) and Wasatch Front GPS networks for crustal deformation in and around the southern Intermountain seismic belt, *Seismol. Res. Lett.*, *69*(2), 159.

Bennett, R. A., J. L. Davis, and B. P. Wernicke (1999), Present-day pattern of Cordilleran deformation in the western United States, *Geology*, *27*(4), 371–374.

Bennett, R. A., J. L. Davis, J. E. Normandeau, and B. P. Wernicke (2002), Space geodetic measurements of plate boundary deformation in the western U.S. Cordillera, in *Plate Boundary Zones*, *Geodyn. Ser.*, vol. 30, edited by S. Stein and J. Freymueller, pp. 27–55, AGU, Washington, D. C.

Bennett, R. A., B. P. Wernicke, N. A. Niemi, A. M. Friedrich, and J. L. Davis (2003), Contemporary strain rates in the northern Basin and Range province from GPS data, *Tectonics*, *22*(2), 1008, doi:10.1029/2001TC001355.

Beutler, G., I. Mueller, and R. Neilan (1994), The International GPS Service for geodynamics: Development and start of official service on January 1, 1994, *Bull. Geod.*, *68*, 39–70.

Bock, Y., et al. (1997), Southern California permanent GPS geodetic array: Continuous measurements of regional crustal deformation between the Landers and Northridge earthquakes, *J. Geophys. Res.*, *102*, 18,103–18,033.

Boore, D. M., and D. P. Hill (1973), Wave propagation characteristics in the vicinity of the San Andreas fault, in *Proceedings of the Conference on Tectonic Problems of the San Andreas Fault System*, edited by L. Kovach and A. Nur, *Stanford Univ. Publ. Geol. Sci.*, *13*, 215–224.

Bos, A. G., W. Spakman, and M. C. J. Nyst (2003), Surface deformation and tectonic setting of taiwan inferred from a GPS velocity field, *J. Geophys. Res.*, *108*(B10), 2458, doi:10.1029/2002JB002336.

Chinnery, M. A. (1970), Earthquake displacement fields, in *Earthquake Displacement Fields and the Rotation of the Earth*, edited by L. Mansinha, pp. 17–38, Springer, New York.

DeMets, C., D. Gordon, D. F. Argus, and S. Stein (1990), Current plate motions, *Geophys. J. Int.*, *101*, 425–478.

DeMets, C., D. Gordon, D. F. Argus, and S. Stein (1994), Effect of recent revisions to the geomagnetic reversal time scale on estimates of current plate motion, *Geophys. Res. Lett.*, *21*, 2191–2194.

Dixon, T. H., S. Robaudo, J. Lee, and M. C. Reheis (1995), Constraints on present-day Basin and Range deformation from space geodesy, *Tectonics*, *14*(4), 755–772.

Dixon, T. H., F. Farina, C. DeMets, F. Suarez Vidal, J. Fletcher, B. Marquez Azua, M. M. Miller, O. Sanchez, and P. Umhoefer (2000a), New kinematic models for Pacific-North America motion from 3 Ma to Present: 2. Evidence for a "Baja California shear zone", *Geophys. Res. Lett.*, *27*, 3961–3964.

Dixon, T. H., M. Miller, F. Farina, H. Wang, and D. Johnson (2000b), Present-day motion of the Sierra Nevada block and some tectonic implications for the Basin and Range province, North American Cordillera, *Tectonics*, *19*, 1–24.

Dokka, R. K., and C. J. Travis (1990), Role of the eastern California shear zone in accommodating Pacific-North America plate motion, *Geophys. Res. Lett.*, *17*, 1323–1326.

Eberhart-Phillips, D., and A. J. Michael (1993), Three-dimensional velocity structure, seismicity, and fault structure in the Parkfield region, central California, *J. Geophys. Res.*, *98*, 15,737–15,758.

Eberhart-Phillips, D., M. Lisowski, and M. D. Zoback (1990), Crustal strain near the Big Bend of the San Andreas fault: Analysis of the Los Padres-Tehachapi trilateration networks, California, *J. Geophys. Res.*, *95*, 1139–1153.

Engdahl, E. R., R. D. Van der Hilst, and R. P. Buland (1998), Global teleseismic earthquake relocation with improved travel times and procedures for depth determination, *Bull. Seismol. Soc. Am.*, *88*, 722–743.

England, P., and G. Houseman (1989), Extension during continental convergence, with application to the Tibetan Plateau, *J. Geophys. Res.*, *94*, 17,561–17,579.

Flesch, L. M., W. E. Holt, A. J. Haines, and B. Shen-Tu (2000), Dynamics of the Pacific-North American plate boundary in the western United States, *Science*, *287*, 834–836.

Friedrich, A. M., B. P. Wernicke, N. A. Niemi, R. A. Bennett, and J. L. Davis (2003), Comparison of geodetic and geologic data from the Wasatch region Utah, and implications for the spectral character of Earth deformation at periods 10 to 10 million years, *J. Geophys. Res.*, *108*(B4), 2199, doi:10.1029/2001JB000682.

Gan, W. J., L. Svarc, C. Savage, and W. H. Prescott (2000), Strain accumulation across the Eastern California shear zone at latitude 36°30′N, *J. Geophys. Res.*, *105*, 16,229–16,236.

Healy, J. H., and L. G. Peake (1975), Seismic velocity structure along a section of the San Andreas fault near Bear Valley California, *Bull. Seismol. Soc. Am.*, *65*, 1177–1197.

Huggett, G. R., L. E. Slater, and J. Langbein (1977), Fault episodes near Hollister, California: Initial results using a multiwavelength distance-measuring instrument, *J. Geophys. Res.*, *82*, 3361–3368.

Jackson, D. D., Z.-K. Shen, D. Potter, X.-B. Ge, and L.-Y. Sung (1997), Southern California deformation, *Science*, *277*, 1621–1622.

Jackson, J., and P. Molnar (1990), Active faulting and block rotations in the western Transverse Ranges, California, *J. Geophys. Res.*, *95*, 22,073–22,087.

Kanamori, H. (1977), The energy release in great earthquakes, *J. Geophys. Res.*, *82*, 2981–2987.

King, G., D. Oppenheimer, and F. Amelung (1994), Block versus continuum deformation in the western United States, *Earth Planet. Sci. Lett.*, *128*, 55–64.

King, N. E., J. L. Svarc, E. Fogelman, W. K. Gross, K. W. Clark, G. D. Hamilton, C. H. Stiffler, and J. M. Sutton (1995), Continuous GPS observations across the Hayward fault, California, 1991–1994, *J. Geophys. Res.*, *100*, 20,271–20,283.

Kostrov, V. V. (1974), Seismic moment and energy of earthquakes, and seismic flow of rock, *Earth Phys.*, *1*, 23–40.

Lachenbruch, A. H., J. H. Sass, and P. Morgan (1994), Thermal regime of the southern Basin and Range province: 2. Implications of heat flow for regional extension and metamorphic core complexes, *J. Geophys. Res.*, *99*, 22,121–22,133.

Lienkaemper, J., G. Borchardt, and M. Lisowski (1991), Historic creep rate and potential for seismic slip along the Hayward fault, California, *J. Geophys. Res.*, *96*, 18,261–18,283.

Lyons, S., and D. Sandwell (2003), Fault creep along the southern San Andreas from interferometric synthetic aperture radar, permanent scatterers, and stacking, *J. Geophys. Res.*, *108*(B1), 2047, doi:10.1029/2002JB001831.

Lyons, S. N., Y. Bock, and D. T. Sandwell (2002), Creep along the Imperial fault, southern California, from GPS measurements, *J. Geophys. Res.*, *107*(B10), 2249, doi:10.1029/2001JB000763.

Mahrer, K. D., and A. Nur (1979), Static strike-slip faulting in a horizontally varying crust, *Bull. Seismol. Soc. Am.*, *69*, 975–1009.

Malservisi, R., K. P. Furlong, and T. H. Dixon (2001), Influence of the earthquake cycle and lithospheric rheology on the dynamics of the eastern California shear zone, *Geophys. Res. Lett.*, *28*, 2731–2734.

Miller, M. M., D. J. Johnson, T. H. Dixon, and R. K. Dokka (2001), Refined kinematics of the Eastern California shear zone from GPS observations, 1993–1998, *J. Geophys. Res.*, *106*, 2245–2263.

Nalbant, S. S., A. Hubert, and G. C. P. King (1998), Stress coupling between earthquakes in northwest Turkey and the north Aegean Sea, *J. Geophys. Res.*, *103*, 24,469–24,486.

Nicholson, C., L. Seeber, P. Williams, and L. R. Sykes (1986), Seismicity and fault kinematics through the eastern Transverse Ranges, California: Block rotation, strike-slip faulting and low-angle thrusts, *J. Geophys. Res.*, *91*, 4891–4908.

Oldow, J. S., C. L. V. Aiken, J. L. Hare, J. F. Ferguson, and R. F. Hardyman (2001), Active displacement transfer and differential block motion within the central Walker Lane, western Great Basin, *Geology*, *29*(1), 19–22.

Parsons, T., S. Toda, R. S. Stein, A. Barka, and J. H. Dieterich (2000), Heightened odds of large earthquakes near Istanbul: An interaction-based probability calculation, *Science*, *288*, 661–665.

Rosen, P., W. E. Fielding, S. Hensley, S. Buckley, and P. Vincent (1998), Aseismic creep along the San Andreas fault northwest of Parkfield, CA measured by radar interferometry, *Geophys. Res. Lett.*, *26*, 825–828.

Rybicki, K. (1978), Static deformation of a laterally inhomogeneous halfspace by a two-dimensional strike-slip fault, *J. Phys. Earth*, *26*, 351–366.

Sass, J. H., A. H. Lachenbruch, S. P. Galanis Jr., P. Morgan, S. S. Priest, T. H. Moses Jr., and R. J. Munroe (1994), Thermal regime of the southern Basin and Range province: 1. Heat flow data from Arizona and the Mojave Desert of California and Nevada, *J. Geophys. Res.*, *99*, 22,093–22,119.

Sauber, J., W. Thatcher, S. C. Solomon, and M. Lisowski (1994), Geodetic slip rate for the eastern California shear zone and the recurrence time of Mojave Desert earthquakes, *Nature*, *367*, 264–266.

Savage, J. C., M. Lisowski, and W. Prescott (1990), An apparent shearzone trending north-northwest across the Mojave Desert into Owens Valley, *Geophys. Res. Lett.*, *17*, 2113–2116.

Savage, J. C., M. Lisowski, J. L. Svarc, and W. K. Gross (1995), Strain accumulation across the central Nevada seismic zone, 1973–1994, *J. Geophys. Res.*, *100*, 20,257–20,269.

Schulz, S. S., G. M. Mavko, R. O. Burford, and W. D. Stuart (1982), Long-term fault creep observations in central California, *J. Geophys. Res.*, *87*, 6977–6982.

Segall, P., and R. Harris (1987), Earthquake deformation cycle on the San Andreas fault near Parkfield, California, *J. Geophys. Res.*, *92*, 10,511–10,525.

Shen, Z.-K., D. D. Jackson, and B.-X. Ge (1996), Crustal deformation across and beyond the Los Angeles basin from geodetic measurements, *J. Geophys. Res.*, *101*, 27,957–27,980.

Shen-Tu, B., W. E. Holt, and A. J. Haines (1998), Contemporary kinematics of the western United States determined from earthquake moment tensors, very long baseline interferometry, and GPS observations, *J. Geophys. Res.*, *103*, 18,087–18,117.

Shen-Tu, B., W. E. Holt, and A. J. Haines (1999), Deformation kinematics in the western United States determined from Quartenary fault slip rates and recent geodetic data, *J. Geophys. Res.*, *104*, 28,927–28,955.

Shewchuk, J. R. (1996), Triangle: Engineering a 2D quality mesh generator and Delaunay triangulator, paper presented at First Workshop on Applied Computational Geometry, Assoc. for Comput. Mach., Philadelphia, Pa.

Snay, R. A., M. W. Cline, C. R. Philipp, D. D. Jackson, Y. Feng, Z.-K. Shen, and M. Lisowski (1996), Crustal velocity field near the big bend of California's San Andreas fault, *J. Geophys. Res.*, *101*, 3173–3185.

Spakman, W., and M. C. J. Nyst (2002), Inversion of relative motion data for fault slip and continuous deformation in crustal blocks, *Earth Planet. Sci. Lett.*, *203*, 577–591.

Stewart, J. H. (1971), Basin and Range structure: A system of horsts and grabens produced by deep-seated extension, *Geol. Soc. Am. Bull.*, *82*, 1019–1044.

Thatcher, W., G. R. Foulger, B. R. Julian, J. Svarc, E. Quilty, and G. W. Bawden (1999), Present-day deformation across the Basin and Range province, western United States, *Science*, *283*, 1714–1718.

Thatcher, W., and T. C. Hanks (1973), Source parameters of southern Californian earthquakes, *J. Geophys. Res.*, *78*, 8547–8576.

Unruh, J. R., and W. R. Lettis (1998), Kinematics of transpressional deformation in the eastern San Francisco Bay region, California, *Geology*, *26*(1), 19–22.

Ward, S. N. (1998), On the consistency of earthquake moment rates, geological fault data and space geodetic strain: The United States, *Geophys. J. Int.*, *134*, 172–186.

Wdowinsky, S., Y. Sudman, and Y. Bock (2001), Geodetic detection of active faults in S. California, *Geophys. Res. Lett.*, *28*, 2321–2324.

Wernicke, B., A. M. Friedrich, N. A. Niemi, R. A. Bennett, and J. L. Davis (2000), Dynamics of plate boundary fault systems from Basin and Range geodetic network BARGEN and geological data, *GSA Today*, *10*(11), 1–7.

Working Group on California Earthquake Prediction (WGCEP) (1995), Seismic hazards in southern California: Probable earthquakes, 1994 to 2024, *Bull. Seismol. Soc. Am.*, *85*, 379–439.

A. G. Bos and W. Spakman, Faculty of Earth Sciences, Utrecht University, Budapestlaan 4, NL-3584 CD Utrecht, Netherlands. (bos@geo.uu.nl; wims@geo.uu.nl)